A high contrast and resolution reconstruction algorithm in quantitative photoacoustic tomography*

Anwesa Dey † Alfio Borzì ‡ Souvik Roy §

Abstract

A framework for reconstruction of optical diffusion and absorption coefficients in quantitative photoacoustic tomography is presented. This framework is based on a Tikhonov-type functional with a regularization term promoting sparsity of the absorption coefficient and a prior involving a Kubelka-Munk absorption-diffusion relation that allows to obtain superior reconstructions. The reconstruction problem is formulated as the minimization of this functional subject to the differential constraint given by a photon-propagation model. The solution of this problem is obtained by a fast and robust sequential quadratic hamiltonian algorithm based on the Pontryagin maximum principle. Results of several numerical experiments demonstrate that the proposed computational strategy is able to obtain reconstructions of the optical coefficients with high contrast and resolution for a wide variety of objects.

Keywords: Quantitative photoacoustic tomography, nonsmooth PDE optimization, Pontryagin maximum principle, sequential quadratic hamiltonian algorithm.

MSC: 35R30, 49J20, 49K20, 65M08, 82C31

1 Introduction

Photoacoustic tomography (PAT) is an emerging hybrid imaging technique that combines two imaging modalities: optical tomography, with a large contrast of optical parameters in an object, and ultrasound imaging, which provides high resolution images. The PAT technique is based on the photoacoustic effect where an object is exposed to a short-pulse optical radiation that propagates through it and is, in part, partially absorbed. This phenomenon leads to heating and

*Partially supported by the BMBF-Project iDeLIVER : Intelligent MR Diagnosis of the Liver by Linking Model and Data-driven Processes, US National Science Foundation Grant No: 2309491, and University of Texas at Arlington, Research Enhancement Program Grant No: 2022-605.

†anwesary@math.utah.edu, Department of Mathematics, University of Utah, John A. Widtsoe Building 155 S 1400 E, Salt Lake City, 84112, Utah, USA.

‡alfio.borzi@mathematik.uni-wuerzburg.de, Institut für Mathematik, Universität Würzburg, Emil-Fischer-Strasse 30, 97074 Würzburg, Germany.

§souvik.roy@uta.edu, Department of Mathematics, University of Texas at Arlington, 411 S. Nedderman Drive, Arlington, 76019, Texas, USA.

thermal expansion of the region where the propagation occurs, so that acoustic pulses are emitted that travel back to the boundary of the object, where they can be measured [61, 63]. From these measured acoustic pulses, one can obtain the initial pressure distribution and, subsequently, optical coefficients like the absorption and diffusion, through the formulation of inverse problems.

The reconstruction of the initial pressure distribution denoted with $\mathcal{H}(x),\ x \in \Omega \subset \mathbb{R}^n$, from the measured acoustic pulses on the boundary of the object $\partial\Omega$, can be formulated as an inverse source problem for the wave operator as follows: Let $p(x,t)$ and $\mathcal{C}(x)$ denote the pressure and the speed of the acoustic wave, respectively. Then p satisfies the following equation

$$\begin{aligned} &p_{tt} - \mathcal{C}^2(x)\,\Delta p = 0, \quad (x,t) \in \Omega \times [0,T] \\ &p(x,0) = \mathcal{H}(x), \quad x \in \Omega \\ &\frac{\partial p}{\partial t}(x,0) = 0, \quad x \in \Omega \end{aligned} \tag{1}$$

where T represents the time period of propagation of the acoustic waves starting with the initial pressure field $\mathcal{H}$. Then, the time-dependent acoustic wave signals of the form

$$p(x,t),\ \frac{\partial p}{\partial n}(x,t) \quad (x,t) \in \partial\Omega \times [0,T] \tag{2}$$

are measured at the acquisition boundary $\partial\Omega$. The inverse problem is to recover $\mathcal{H}$ given the data in (2). This is also known as the classical PAT inverse problem [10, 11, 12, 13, 25, 31]

The aforementioned inverse problem has been very well studied; see, e.g., [25, 31], and the solution to this problem gives the initial pressure distribution $\mathcal{H}$ profile in the entire domain Ω. However, this procedure does not give information about the more specific properties of the object like the optical parameters of absorption and diffusion coefficient. Thus, to reconstruct the optical parameters from the initial pressure distribution, a second inverse problem is solved, which is known as quantitative photoacoustic tomography (QPAT). One of the major applications of QPAT is to provide accurate images of the heart for the study of congenital heart diseases [32]. Other applications of QPAT include detecting cancerous tissues, thus facilitating biomedical studies [34, 51]. Notice that there are other optical imaging methods that have a structure similar to QPAT in the sense that these methods make use of the photoacoustic effect to determine specific internal features in an object. For example, the fluorescence optical diffuse tomography (FDOT), which is used to detect fluorescing targets in tissues [46, 53].

However, in QPAT and similar modalities, the accurate reconstruction of the optical parameters poses several theoretical and computational challenges that are under investigation by many research groups. Our purpose is to contribute to this research work with a novel QPAT reconstruction framework with high resolution and high contrast, which is of paramount importance especially in the context of biomedical imaging for detection of cancerous tissues.

Mathematically, the initial pressure distribution $\mathcal{H}(x)$ is a function of the absorption coefficient $\sigma_a(x)$, of the intensity of radiation $u(x)$, and of the Grüneisen coefficient $\Gamma(x)$, which measures the amount of ultrasound generated by the absorbed radiation at the point x. In general, the intensity of radiation u is a function of space and time and its evolution is governed by the radiative transfer equation (RTE) (see e.g., [9, Section 3.2], [38, Chapter 7], [51]). However, assuming the use of short light pulses such that the radiation propagates for a very short time at the scale of small acoustic wave lengths, we have that the scattering is significantly larger than absorption (see [38, Chapter 9], [9, Section 3.3]). Thus, the photons are scattered almost uniformly in all directions

leading to an almost uniform angular distribution. This phenomenon is prevalent inside biological tissues [30, 51] and blood [38, Chapter 9]. In this case, it has been shown in [9, Sec 3.3] that the photon current satisfies a steady state assumption, which results in the diffusion approximation of the RTE equation. Therefore, in this setting, the intensity of radiation $u(x)$ is modelled by the following diffusion equation [11, 12, 13]:

$$\begin{aligned} -\nabla \cdot D(x)\,\nabla u(x) + \sigma_a(x)\,u(x) = 0, \qquad & \text{in } \Omega, \\ u(x) = g(x), \qquad & \text{on } \partial\Omega, \end{aligned}$$

where g is the known intensity of the radiation that is applied at the boundary of the object. In this framework, the initial pressure distribution function is given by

$$\mathcal{H}(x) = \Gamma(x)\,\sigma_a(x)\,u(x), \quad x \in \Omega.$$

The QPAT inverse problem requires to recover the absorption coefficient $\sigma_a(x)$ and the diffusion coefficient $D(x)$, given $\mathcal{H}$ and g.

There are several works related to theoretical and computational frameworks for reconstructions in QPAT; see, e.g.,[11, 15, 33, 36, 64]. In the work [13], it has been shown that, if Γ is given, then the coefficients (D, σ_a) can be uniquely and stably reconstructed based on two different sets of initial pressure distribution data generated by two well-chosen boundary conditions g_1 and g_2 for two copies of the diffusion equation given above. Also in [13], we find a method for reconstruction that relies on the solution of a set of transport and elliptic equations. Further, in [11, 12] it has been shown that all three parameters (D, σ_a, Γ) cannot be reconstructed simultaneously, irrespective of the number of illuminations unless one considers the QPAT inversion problem at different wavelengths. The correspondence between the QPAT inversion problem and parameter estimation with PDE's was illustrated in [14]. Other works on QPAT include: the multiple-source framework in [65], and its analysis [54], a PDE-optimization framework using the radiative transfer equation [1], the recovery of absorption coefficient of a small absorber [8], the reconstruction of absorption and scattering coefficients [59], and the analysis of the linearised QPAT problem [36].

In addition to the theoretical investigation of the QPAT problem, there are several numerical reconstruction algorithms for solving related inversion problems. In [24], the authors develop an iterative method using the radiation map to reconstruct the optical parameters. A non-linear model-based inversion scheme was formulated in [43] for determining chromophore concentrations in 2D. In [52], a gradient-based scheme for QPAT using the radiative transfer equation is discussed. A new iterative reconstruction algorithm using a different form of the radiation function and Robin-boundary data was proposed in [47]. It appears from the simulation results in these works that existing algorithms for QPAT have difficulties in reconstructing accurately both D and σ_a. Furthermore, these algorithms do not perform well to reconstruct the optical coefficients with high contrast, which is an inherent property of tissues, thus limiting their range of applicability in biomedical problems.

One of the major reason for the poor reconstruction of D is due to the fact that the initial pressure distribution data does not directly contain information on D. On the other hand, it has been shown that there is a relation between D and σ_a and the reduced scattering coefficient σ_s, which is given by [6, 27]

$$D = \frac{1}{3(\sigma_a + \sigma_s)}. \tag{3}$$

This fact shows a deficiency in the use of the diffusion approximation for reconstructing D, which would require to employ the radiative transfer (or transport) equation (RTE) [38] as the adequate model for light transport in tissues. Therefore, although the main point in photo acoustic is a thermodynamics phenomenon that explains how absorbed energy is transformed in a pressure wave, also scattering is relevant for a successful reconstruction of the diffusion coefficient, as it is illustrated by results in, e.g., [59].

However, in some applications a proportionality between σ_a and σ_s appears. In particular, the following relation between σ_a and σ_s has for long been described by the Kubelka-Munk theory in the diffusive regime [41, 37, 62, 28, 48, 29]. We have

$$\sigma_s = \frac{2R_\infty}{(1-R_\infty)^2}\sigma_a, \tag{4}$$

where R_∞ is the diffuse reflectance of the biological object. In the near infrared wavelength region, $\mathbb{R}_\infty$ has been experimentally found to be lying somewhere in the range of 0.5-1.25 (see Figure 4 in [29]). Furthermore, a similar linear relation between σ_a and σ_s has also been found to be experimentally true for the tissues of brain, breast, heart, lungs, bone, prostate and tumor; see, e.g., [26, 51], and Table 1, where we report measured values of the absorption and reduced scattering coefficients for various human tissues.

Table 1: Values of the absorption and the reduced scattering coefficients for various tissues at the near-infrared wavelengths [51].

Tissue	Wavelength (nm)	σ_a (cm^{-1})	σ_s (cm^{-1})
Brain	760	0.11-0.17	4.0-10.5
Breast	760	0.031-0.1	8.3-12.0
Heart	661	0.12-0.18	5.22-90.80
Lungs	661	0.49-0.88	21.14-22.52
Bone	760	0.07-0.09	11.9-14.1
Prostate	732	0.09-0.72	3.37-29.8
Tumor	795	0.068-0.102	12.4-13.1

These results suggest that the reconstruction of the diffusion coefficient in the framework of the diffusion approximation can be improved if we include our qualitative prior knowledge represented by (3) and (4) in the formulation of our inverse problem.

For this purpose, based on the results given in Table 1 and supported by the Kubelka-Munk relation, we construct our prior based on the following tentative relation between the absorption and the reduced scattering coefficients

$$\sigma_s \approx c\ \sigma_a. \tag{5}$$

This choice is based on results of measurements indicating that the value of c varies among different biological tissues in the approximate range $(30, 800)$. Notice that in our approach we interpret (5) as a mean approximate relation between σ_a and σ_s in the tissues (with the value of c arbitrarily chosen in a given interval determined by the application) and aim at using this information for better reconstruction of the QPAT coefficients.

We demonstrate that the consistent use of (3) and (5) embedded as a prior in our nonsmooth optimization problem results in a novel reconstruction strategy that allows to obtain reconstructions of D and σ_a with high resolution and high contrast. However, it is important to emphasize that the high-quality reconstructions that we obtain do not necessarily satisfy the relations (3) and (5). On the other hand, we show that our computational framework is certainly valid for biomedical applications with near-infrared light illumination of tissues in order to accurately detect the cancerous ones inside the organs mentioned in Table 1, where the Kubelka-Munk relation (5) holds approximately true.

In our problem formulation, we consider the minimization of a Tikhonov-type least squares functional with regularization terms including the relation between D and σ_a mentioned above. Further, we include terms that promote sparsity in the reconstruction, in order to accommodate the fact that, in biomedical application, different tissues appear distributed as almost non-overlapping bounded regions of the domain under consideration. However, while the introduction of nonsmooth penalization terms in the functional considerably contribute to the ability of our method to provide sharp reconstructions as in [2, 49], they require the development of sophisticated optimization techniques that apply in the nonsmooth case. We refer to [56] for a work that pioneered the use of L^1 penalization terms to promote sparsity in PDE optimization and the development of semi-smooth Newton (SSN) methods to solve the corresponding problems. On the other hand, the implementation of a SSN scheme requires the application of the Hessian of the optimization problem and, for this purpose, in addition to solving the model equation and its adjoint, one needs to solve other two linearized equations. This fact and further implementation issues make the development of the SSN scheme difficult to practitioners.

To overcome these difficulties, we extend the sequential quadratic hamiltonian (SQH) algorithm, proposed in [18, 19, 20] for nonsmooth PDE optimal control problems, to solve our inverse problem. This algorithm is based on the Pontryagin maximum principle (PMP), which is well-known in the theory of optimal control of dynamical systems. Our focus on the SQH algorithm is motivated by the fact that it is easy to implement, it appears very efficient and robust, and it is wellposed as an iterative scheme [18, 19]. A specific feature of the iterative SQH method is that it relies on a pointwise optimization procedure.

Several numerical experiments are performed to demonstrate the computational effectiveness of our methodology. The results of these experiments show that our QPAT inverse problem, which includes a prior relation on D and σ_a, and the SQH algorithm solving this problem, result in a fast and accurate reconstruction procedure. These are the main novelties of our work.

This paper is organized as follows. In the next section, we discuss our optimization formulation of the QPAT inverse problem, and illustrate our use of a relation between D and σ. Further, we discuss L^2 and L^1 penalization terms. In Section 3, we provide theoretical consideration on solutions to our minimization problem and discuss their characterization in the PMP framework. Section 4 is devoted to illustrating all details of our numerical optimization procedure that includes wellposedness of the SQH algorithm and the numerical approximation of our PDE governing model and of its optimization adjoint. In Section 5, results of numerical experiments are presented that successfully validate our QPAT framework. For this purpose, different test cases with synthetic data are considered that allow to investigate the role of the optimization parameters and the ability of our computational framework to provide reconstructions of the coefficients D and σ with high contrast and resolution, also in the case of data affected by noise. A section of conclusions completes this work.

2 Formulation of a QPAT optimization problem

We start discussing the governing model of our QPAT inverse problem. For this purpose, we specify the dimension $n = 2$, and refer to the set of coordinates (x, y). Let $u(x, y)$ be the total number of photons at a point (x, y) inside an object represented by the domain Ω. In our discussion, Ω is either a rectangle or a convex subset of $\mathbb{R}^2$ with boundary $\partial\Omega$ of class C^2. We assume that u satisfies the following photon-propagation problem

$$\begin{aligned} -\nabla \cdot (D(x,y)\,\nabla u(x,y)) + \sigma_a(x,y)\,u(x,y) = 0, \qquad & (x,y) \in \Omega \\ u(x,y) = g(x,y), \quad & (x,y) \in \partial\Omega, \end{aligned} \tag{6}$$

where $D(x, y) > 0$ represents the diffusion coefficient at (x, y). The non-negative absorption coefficient σ_a is given by

$$\sigma_a(x, y) = \sigma(x, y) + \sigma_b,$$

where σ_b is a known background absorption coefficient and σ represents the deviation from this value in correspondence of organs and sites of tumor. We remark that even though σ is a signed function, however later on, we will impose bounds on σ such that $\sigma_a > 0$. Further, the function g represents the known intensity of radiation at the boundary of the object. For the reconstruction of D and σ_a, we require the knowledge, by measurements, of the optical energy given by

$$\mathcal{H}(x, y, \sigma, u_i) = \Gamma\,(\sigma(x, y) + \sigma_b)\,u_i(x, y), \qquad i = 1, 2, \tag{7}$$

for two sets of boundary radiation functions g_i, where Γ is the known Grüneisen coefficient that is assumed to be a known constant.

Our QPAT inverse problem consists in obtaining the unknown pair (D, σ), given H and g. For this purpose, we formulate a minimization problem with the following cost functional

$$\begin{aligned} J(D, \sigma, u_1, u_2) = \frac{\alpha}{2} \sum_{i=1}^{2} \int_\Omega (\mathcal{H}(x, y, \sigma, u_i) - G_i^\delta(x, y))^2 \, dxdy + \frac{\xi_1}{2} \int_\Omega \sigma^2(x, y) \, dxdy \\ + \frac{\xi_2}{2} \int_\Omega \left(D(x, y) - \frac{1}{3c\,(\sigma(x, y) + \sigma_b)} \right)^2 dxdy + \gamma \int_\Omega |\sigma(x, y)| \, dxdy, \end{aligned} \tag{8}$$

where $G_i^\delta \in L^\infty(\Omega)$ is a given noisy measurement function of the initial pressure distribution corresponding to the boundary radiation functions g_i, $i = 1, 2$. Therefore the first term in the objective functional J represents a least-squares data fit of the initial pressure distribution measurements. We assume that the background value of the absorption coefficient σ_b is known and therefore σ equals zero in the background. In this setting, it is reasonable to introduce a L^2 and L^1 regularization of σ, which result in the second and last terms in (8). In particular, the L^1 term promotes sparsity of σ, thus enhancing contrast.

One novelty of our work is the prior given by the third term in (8). To explain this term, we recall (3) and the related discussion. Hence, by assuming $c \in [30, 800]$, we can make the following approximation

$$3\,(\sigma_a + \sigma_s) \approx 3\,(\sigma_a + c\sigma_a) \approx 3c\sigma_a.$$

We remark that even though we will be choosing $c \in [30, 800]$ in our numerical experiments, the choice of c is not essential. Thus, we employ the following function as prior for the diffusion

coefficient D

$$D(x,y) \approx \bar{D} := \frac{1}{3c\ (\sigma(x,y)+\sigma_b)}. \tag{9}$$

Therefore the third term in J measures the deviation of D in the tissues and tumors from $\bar{D}$.

Our QPAT optimization problem is stated as follows

$$\begin{aligned} &\min_{D,\sigma\in D_{ad}\times\Sigma_{ad}} J(D,\sigma,u_1,u_2) \\ \text{s.t.} \quad &\mathcal{L}(u_1,D,\sigma,g_1)=0, \\ &\mathcal{L}(u_2,D,\sigma,g_2)=0, \end{aligned} \tag{10}$$

('s.t.' means 'subject to') where $\mathcal{L}(u_i,D,\sigma,g_i)=0$, $i=1,2$, denote (6) for the boundary radiation functions g_i, $i=1,2$, respectively, and our aim is to recover D and σ in the following admissible sets

$$\begin{aligned} D_{ad} &= \{D\in L^2(\Omega) : 0<D_l\le D(x,y)\le D_r, \text{ a.e. in } \Omega\}, \\ \Sigma_{ad} &= \{\sigma\in L^2(\Omega) : \sigma_l\le \sigma(x,y)\le \sigma_r, \text{ a.e. in } \Omega,\}, \end{aligned} \tag{11}$$

where σ_l is chosen such that the total absorption coefficient $\sigma_a=\sigma+\sigma_b>0$, e.g., one can choose $\sigma_l=-\sigma_b+\sigma_\epsilon$, with σ_ϵ a small positive number.

3 Analysis of the QPAT inverse problem

We remark that our diffusion model (6), with the given bounds on the coefficients and Dirichlet boundary conditions, is a well-studied problem and we refer to [35, 42] for two classical references. Specifically, one can verify that with $D\in D_{ad}$ and $\sigma\in\Sigma_{ad}$ our operator is uniformly elliptic and the boundedness conditions on the coefficients required in, e.g., [35] are satisfied. Then, assuming that the Dirichlet data g corresponds to the trace of a $H^1(\Omega)$ function, the following proposition holds whose proof can be found e.g., in [42].

Proposition 1. *Let $D\in D_{ad}$, $\sigma\in\Sigma_{ad}$. Then there exists a unique solution $u\in H^1(\Omega)$ to (6).*

Additional regularity of the solution, that is, $u\in H^1(\Omega)\cap H^2(\Omega)$, is attained at the interior of Ω if D is assumed Lipschitz continuous, and this regularity holds globally if $\partial\Omega$ is of class C^2; see [35]. Further results can be found in, e.g., [3]. In particular, we refer to [22, 45] for the problem of establishing boundedness of the gradient of solutions to the diffusion model.

With Proposition 1, we have that the map $(D,\sigma)\mapsto u=u(D,\sigma)$, where u is the solution to (6) for given $(D,\sigma)\in D_{ad}\times\Sigma_{ad}\subset L^\infty(\Omega)\times L^\infty(\Omega)$, is well defined. Furthermore, this map is continuous as shown below; see also [40].

Lemma 3.1. *Let $\Omega\subset\mathbb{R}^2$ and consider any two pairs (u_1,D_1,σ_1), $(u_2,D_2,\sigma_2)\in H^1(\Omega)\times D_{ad}\times\Sigma_{ad}$ that satisfy (6) with g the trace of a $H^1(\Omega)$ function. Then the following estimate holds*

$$\|u_1-u_2\|_{H^1(\Omega)}\le C_1\left(\|D_1-D_2\|_{L^\infty(\Omega)}+\|\sigma_1-\sigma_2\|_{L^\infty(\Omega)}\right).$$

Furthermore, if for the given pairs the gradient of u_1 (respectively u_2), is essentially bounded, then the following estimate holds

$$\|u_1-u_2\|_{H^1(\Omega)}\le C_2\left(\|D_1-D_2\|_{L^2(\Omega)}+\|\sigma_1-\sigma_2\|_{L^2(\Omega)}\right).$$

Proof. The two pairs satisfy both the diffusion equation in weak form. We have

$$(D_i \nabla u_i, \nabla v) + (\tilde{\sigma}_i u_i, v) = 0, \qquad v \in H_0^1(\Omega),$$

where $\tilde{\sigma}_i = \sigma_i + \sigma_b$ and $u_i = g$ on the boundary, $i = 1, 2$.

Therefore we have

$$(D_1 \nabla u_1, \nabla v) + (\tilde{\sigma}_1 u_1, v) = (D_2 \nabla u_2, \nabla v) + (\tilde{\sigma}_2 u_2, v).$$

Thus, by algebraic manipulation, we obtain

$$(D_1 [\nabla u_1 - \nabla u_2], \nabla v) + (\tilde{\sigma}_1 [u_1 - u_2], v) = ([D_2 - D_1] \nabla u_2, \nabla v) + ([\sigma_2 - \sigma_1] u_2, v).$$

In particular, taking $v = u_1 - u_2$, we have

$$\begin{aligned}&(D_1 \nabla [u_1 - u_2], \nabla [u_1 - u_2]) + (\tilde{\sigma}_1 [u_1 - u_2], [u_1 - u_2]) \\ &= ([D_2 - D_1] \nabla u_2, \nabla [u_1 - u_2]) + ([\sigma_2 - \sigma_1] u_2, [u_1 - u_2]).\end{aligned}$$

Since $D_i \in D_{ad}$ and $\sigma_i \in \Sigma_{ad}$, we have

$$c_1 \|u_1 - u_2\|^2_{H^1(\Omega)} \leq ([D_2 - D_1] \nabla u_2, \nabla [u_1 - u_2]) + ([\sigma_2 - \sigma_1] u_2, [u_1 - u_2]).$$

where $c_1 = \min\{D_l, \sigma_l + \sigma_b\}$. Hence, considering that both D and σ are bounded, we have the estimate

$$c_1 \|u_1 - u_2\|_{H^1(\Omega)} \leq c_2 \left(\|D_1 - D_2\|_{L^\infty(\Omega)} + \|\sigma_1 - \sigma_2\|_{L^\infty(\Omega)}\right),$$

where $c_2 = \max\{\|u_2\|_{L^2(\Omega)}, \|\nabla u_2\|_{L^2(\Omega)}\}$. Hence, the first statement of the lemma is proved with $C_1 = c_2/c_1$.

Further, by the assumption that $\|\nabla u_2\|_{L^\infty(\Omega)} \leq M$ (resp. $\|\nabla u_1\|_{L^\infty(\Omega)} \leq M$), for some positive constant M, we have

$$\begin{aligned}c_1 \|u_1 - u_2\|^2_{H^1(\Omega)} &\leq \|\nabla u_2\|_{L^\infty(\Omega)} \|D_2 - D_1\|_{L^2(\Omega)} \|\nabla [u_1 - u_2]\|_{L^2(\Omega)} \\ &\quad + \|u_2\|_{L^\infty(\Omega)} \|\sigma_2 - \sigma_1\|_{L^2(\Omega)} \|u_1 - u_2\|_{L^2(\Omega)} \\ &\leq \left(\|\nabla u_2\|_{L^\infty(\Omega)} \|D_2 - D_1\|_{L^2(\Omega)} + \|u_2\|_{L^\infty(\Omega)} \|\sigma_2 - \sigma_1\|_{L^2(\Omega)}\right) \|u_1 - u_2\|_{H^1(\Omega)}\end{aligned}$$

Therefore the claim of the lemma follows from the following result

$$c_1 \|u_1 - u_2\|_{H^1(\Omega)} \leq c_3 \left(\|D_1 - D_2\|_{L^2(\Omega)} + \|\sigma_1 - \sigma_2\|_{L^2(\Omega)}\right),$$

where $c_3 = \max\{\|u_2\|_{L^\infty(\Omega)}, \|\nabla u_2\|_{L^\infty(\Omega)}\}$. Thus, the second statement is proved with $C_2 = c_3/c_1$. □

With this preparation, we can introduce the following reduced cost functional

$$\hat{J}(D, \sigma) = J(D, \sigma, u_1(D, \sigma), u_2(D, \sigma)). \tag{12}$$

Notice that, with this functional, our QPAT optimization problem can be equivalently formulated as the following unconstrained minimization problem

$$\min_{(D,\sigma) \in D_{ad} \times \Sigma_{ad}} \hat{J}(D, \sigma). \tag{13}$$

The proof of existence of a minimizer for (13) by using the classical direct method is a delicate issue since for the minimizing sequences $\{D^k\} \subset L^\infty(\Omega)$ we do not have the strong convergence required to prove fulfilment of the differential constraint (6) in the limit of the minimizing process; see, e.g., Chapter VI of [16] for a related framework. However, this would be possible assuming a compact set of admissible controls, e.g., $\tilde{D}_{ad} = D_{ad} \cap V_l$ where $V_l := \{v \in H^1(\Omega) \,|\, \|v\|_{H^1(\Omega)} \leq l\}$ where l is a given positive constant; see, e.g., [44] for a discussion on this setting. Nevertheless, since these are sufficient and not necessary conditions for existence of an optimal pair (D^*, σ^*), we prefer to work with the admissible sets defined in (11) that appear convenient in applications, and assume existence of the optimal optical coefficients (D^*, σ^*). Our focus is the construction of a method that efficiently computes these coefficients.

Now, concerning the characterization of solutions to our QPAT optimization problem, we can use subdifferential calculus to derive first-order necessary optimality conditions [23, 60]. In particular, if $\hat{J}(D, \sigma)$ is Fréchet differentiable, then the optimal pair (D^*, σ^*) must satisfy

$$\left\langle \nabla \hat{J}(D^*, \sigma^*), (D, \sigma) - (D^*, \sigma^*) \right\rangle \geq 0, \qquad (D, \sigma) \in D_{ad} \times \Sigma_{ad},$$

where $\langle \cdot, \cdot \rangle$ denotes the duality product in L^2.

Alternatively, we can use the Pontryagin maximum principle that can be proven in our case provided that the gradient of the adjoint variable is essentially bounded. However, we can also apply a linearized version of the PMP as discussed in [58]. In both cases, the starting point of the PMP approach is the construction of the Hamiltonian-Pontryagin (HP) function $H : \mathbb{R}^2 \times [D_l, D_r] \times [\sigma_l, \sigma_r] \times \mathbb{R}^4$ that is defined as follows (see [18, 19, 20])

$$\begin{aligned}
&H(x, y, D(x, y), \sigma(x), u_1(x, y), u_2(x, y), q_1(x, y), q_2(x, y)) \\
&= \frac{\alpha}{2} \sum_{i=1}^{2} (\mathcal{H}(x, y, D(x, y), \sigma(x, y), u_i(x, y)) - G_i^\delta(x, y))^2 + \frac{\xi_1}{2} \sigma^2(x, y) \\
&+ \frac{\xi_2}{2} \left(D(x, y) - \bar{D}(x, y) \right)^2 + \gamma |\sigma(x)| \\
&+ \sum_{i=1}^{2} D(x, y) \nabla u_i(x, y) \cdot \nabla q_i(x, y) + \sum_{i=1}^{2} (\sigma(x, y) + \sigma_b)\, u_i(x, y)\, q_i(x, y),
\end{aligned} \tag{14}$$

where $q_i,\ i = 1, 2$ solve the following adjoint equations, which are derived from the Lagrangian and Hamiltonian framework [4]

$$\begin{aligned}
-\nabla \cdot (D(x, y)\, \nabla q_i(x, y))) + (\sigma(x, y) + \sigma_b)\, q_i(x, y) = -\alpha \Gamma\ (\sigma(x, y) + \sigma_b)\, [\mathcal{H}(x, y, \sigma, u_i) - G_i^\delta], \quad \text{in } \Omega \\
q_i(x, y) = 0, \qquad \text{on } \partial\Omega,
\end{aligned} \tag{15}$$

Notice that similar consideration, as for the diffusion model, concerning existence and regularity of solutions apply to these elliptic problems.

Then subject to appropriate conditions the PMP characterization of a minimum of the minimization problem (10) is given by the following theorem (expressed in the equivalent form of a minimum principle)

Theorem 3.1. *Let* $(D^*, \sigma^*, u_1^*, u_2^*)$ *be a solution to* (10). *Then*

$$\begin{aligned} &H(x, y, D^*(x, y), \sigma^*(x, y), u_1^*(x, y), u_2^*(x, y), q_1^*(x, y), q_2^*(x, y)) \\ &= \min_{(v_1, v_2) \in [D_l, D_r] \times [\sigma_l, \sigma_r]} H(x, y, v_1, v_2, u_1^*(x, y), u_2^*(x, y), q_1^*(x, y), q_2^*(x, y)), \end{aligned} \tag{16}$$

for almost all $(x, y) \in \Omega$, *and* u_i^*, $i = 1, 2$ *and* q_i^*, $i = 1, 2$ *solve* (6) *and* (15), *respectively, with* $D = D^*$ *and* $\sigma = \sigma^*$.

We can rewrite condition (16) as follows

$$(D^*(x, y), \sigma^*(x, y)) = \arg\min_{(v_1, v_2) \in [D_l, D_r] \times [\sigma_l, \sigma_r]} H(x, y, v_1, v_2, u_1^*(x, y), u_2^*(x, y), q_1^*(x, y), q_2^*(x, y)). \tag{17}$$

We note that (17) represents a pointwise optimality criteria at each (x, y) and does not involve any derivatives with respect to the optimization variables D and σ. In the next section, we discuss an efficient and robust numerical scheme based on (17) that solves (10) (resp. (13)) to obtain D^* and σ^*.

4 The SQH algorithm for solving the QPAT inverse problem

The sequential quadratic hamiltonian (SQH) algorithm has been proposed in [18, 20], as a new variant of the successive approximations methods; see [21] for an early review. It includes an adaptive quadratic penalty of the updates that results in an augmented Hamiltonian as first proposed in [50]. In this way, an efficient and robust iterative procedure is obtained that is able to solve nonsmooth optimization problems governed by PDEs.

In our SQH implementation, the augmented HP function is given by

$$H_\epsilon(x, y, D, \sigma, \tilde{D}, \tilde{\sigma}, u_1, u_2, q_1, q_2) = H(x, y, D, \sigma, u_1, u_2, q_1, q_2) + \epsilon\,[(D - \tilde{D})^2 + (\sigma - \tilde{\sigma})^2], \tag{18}$$

where $\epsilon > 0$ is a penalization parameter that is chosen adaptively at each step of the SQH iteration process: a larger value of ϵ is chosen if a sufficient decrease of the functional J is not observed while a smaller value of ϵ is chosen if J decreases sufficiently. Specifically, if $\tilde{D}$ and $\tilde{\sigma}$ denote a previous approximation to the diffusion and absorption coefficients sought, then the purpose of quadratic term $\epsilon\,[(D - \tilde{D})^2 + (\sigma - \tilde{\sigma})^2]$ is to have the pointwise minimizer of H_ϵ, and thus an update to D and σ, that is close to the previous values $\tilde{D}$ and $\tilde{\sigma}$ as much as ϵ is large. We also remark that during a step of the optimization problem, that is, for a minimization sweep on all grid points of the (x, y) mesh and, during this process, the values of u and q are those obtained in the previous iteration. The SQH algorithm is given as a pseudocode as follows.

Algorithm 4.1 (SQH algorithm)**.**

1. *Choose* $\epsilon > 0$, $\kappa > 0$, $\lambda > 1$, $\zeta \in (0, 1)$, $\rho \in (0, \infty)$, $(D^0, \sigma^0) \in D_{ad} \times \Sigma_{ad}$
2. *Compute* $u_i^0(D^0, \sigma^0)$ *and* $q_i^0(D^0, \sigma^0, u_i^0)$ *for* $i = 1, 2$. *Set* $k = 0$.

3. *Find* $(D, \sigma) \in D_{ad} \times \Sigma_{ad}$ *such that*

$$H_\epsilon(x, y, D, \sigma, D^k, \sigma^k, u_1^k, u_2^k, q_1^k, q_2^k) = \min_{\substack{w \in [D_l, D_r] \\ z \in [\sigma_l, \sigma_r]}} H_\epsilon(x, y, w, z, D^k, \sigma^k, u_1^k, u_2^k, q_1^k, q_2^k)$$

for all $(x, y) \in \Omega$.

4. *Calculate* $u_i(D, \sigma)$, $i = 1, 2$, *and set* $\tau = \|D - D^k\|^2_{L^2(\Omega)} + \|\sigma - \sigma^k\|^2_{L^2(\Omega)}$.

5. *If* $J(D, \sigma, u_1, u_2) - J(D^k, \sigma^k, u_1^k, u_2^k) > -\rho\,\tau$, *choose* $\epsilon = \lambda\,\epsilon$,
else choose $\epsilon = \zeta\,\epsilon$, $u_i^{k+1} = u_i$, $D^{k+1} = D$, $\sigma^{k+1} = \sigma$, *and calculate the adjoint variables* q_i^{k+1}, $i = 1, 2$, *corresponding to* D^{k+1}, σ^{k+1}, u_i^{k+1}, $i = 1, 2$.

6. *Set* $k = k + 1$

7. *If* $\tau < \kappa$, *STOP and return optimal* (D^k, σ^k) *else go to Step 3.*

8. *end*

The pointwise minimization in Step 3 of this algorithm is carried out by a direct search process, i.e., we divide the domain $[D_l, D_r] \times [\sigma_l, \sigma_r]$ into a two-dimensional discrete grid, evaluate H_ϵ on this grid, and then choose a grid point (w, z) at which H_ϵ is minimum. We remark that in Step 5 of this algorithm, if the inequality $J(D, \sigma, u_1, u_2) - J(D^k, \sigma^k, u_1^k, u_2^k) > -\rho\,\tau$ is true this means that no sufficient decrease of the value of the objective functional J as been achieved. In this case, a larger value of ϵ is taken (since $\lambda > 1$) and the optimization procedure in Step 3. is repeated with the corresponding new augmented HP function. On the other hand, if the inequality above is false, the decrease has met the required criteria for reduction of the value of J, and the new values $D^{k+1} = D$, $\sigma^{k+1} = \sigma$ are obtained. Correspondingly, the updates u_i^{k+1} and q_i^{k+1}, $i = 1, 2$, are computed. In this case, the value of ϵ is reduced by a factor $\zeta < 1$.

The fundamental result required to guarantee wellposedness of the SQH algorithm applied to our QPAT inverse problem is to prove that, if not already at the optimal point, it is always possible to find a value of $\epsilon > 0$ such that the minimization of the corresponding H_ϵ results in new values of D and σ for which the value of the functional J is reduced. We present this result in Theorem 4.1 below and refer to [18, 19] for the use of this theorem for further results on the convergence of the SQH algorithm in a finite number of steps.

Theorem 4.1. *Let* (u_1, u_2, D, σ) *and* $(u_1^k, u_2^k, D^k, \sigma^k)$ *be as in Algorithm 4.1,* $k \in \mathbb{N}_0$, *and denote* $\delta D := D - D^k$, $\delta\sigma := \sigma - \sigma^k$, $\delta u_i := u_i - u_i^k$, $i = 1, 2$. *If the assumptions of Lemma 3.1 are satisfied, then there is a* $\theta > 0$, *independent of* ϵ, k, *and* D^k, σ^k, *such that for the* ϵ *currently chosen by the SQH Algorithm 4.1, it holds that*

$$J(D, \sigma, u_1, u_2) - J(D^k, \sigma^k, u_1^k, u_2^k) < -(\epsilon - \theta)\,\big(\|D - D^k\|^2_{L^2(\Omega)} + \|\sigma - \sigma^k\|^2_{L^2(\Omega)}\big).$$

Proof. See the Appendix. □

For implementing Algorithm 4.1, we need to solve the photon propagation equation (6) for different boundary conditions g_i, $i = 1, 2$, and the corresponding adjoint equations (15). We use a cell-nodal finite-difference scheme, proposed in [7], to discretize (6) and (15). To illustrate

this scheme, we consider the generic form of the equations (6) and (15) defined in the domain $\Omega = (a,b)^2 \subset \mathbb{R}^2$ as follows

$$\begin{aligned} -\nabla \cdot (D(x,y)\nabla u(x,y)) + (\sigma(x,y) + \sigma_b)\, u(x,y) &= f && \text{in } \Omega, \\ u(x,y) &= f_D(x,y) && \text{on } \partial\Omega, \end{aligned} \tag{19}$$

where f and f_D are assumed continuous in Ω and on $\partial\Omega$, respectively. Consider a sequence of uniform grids $\{\Omega_h\}_{h>0}$ given by

$$\Omega_h = \{(x_1^i, x_2^j) \in \mathbb{R}^2 : (x_1^i, x_2^j) = (a+ih, a+jh),\ (i,j) \in \{0,\ldots,N\}^2\} \cap \Omega, \tag{20}$$

where N represents the number of cells in each direction and $h = \dfrac{(b-a)}{N}$ is the mesh size. Then the corresponding cell-nodal discretization places the unknowns u, D, σ at the nodal points (x^i, y^j) of the grid that results in the following approximation of (19) at (x^i, y^j)

$$\begin{aligned} &\frac{1}{h^2}\Big\{ (D_{i+1/2,j} + D_{i-1/2,j} + D_{i,j+1/2} + D_{i,j-1/2})u_{i,j} \\ &- D_{i+1/2,j}u_{i+1,j} - D_{i-1/2,j}u_{i-1,j} - D_{i,j+1/2}u_{i,j+1} - D_{i,j-1/2}u_{i,j-1} \Big\} \\ &+ (\sigma_{i,j} + \sigma_b)u_{i,j} = f_{i,j}, \qquad 1 \le i,j \le N-1. \end{aligned} \tag{21}$$

We denote $D_{i\pm1,j} = D(x^i \pm h, y^j)$, $D_{i,j\pm1} = D(x^j, y^j \pm h)$, and $f_{i,j} = f(x^i, y^j)$. The required intermediate values of D are computed as follows

$$D_{i\pm1/2,j} = \frac{1}{2}\Big(D_{i\pm1,j} + D_{i,j}\Big) \quad \text{and} \quad D_{i,j\pm1/2} = \frac{1}{2}\Big(D_{i,j\pm1} + D_{i,j}\Big).$$

The Dirichlet boundary data f_D is included in the standard way in the right-hand side of the algebraic equation. We use one-sided finite difference discretizations to evaluate the right-hand sides of the adjoint equations. With this discretization scheme in (21), we solve a matrix-vector equation to obtain the unknowns $u_{i,j}$.

5 Numerical results

We present results of numerical experiments to validate the ability of our QPAT optimization framework in the reconstruction of the diffusion coefficient D and the absorption coefficient σ profiles with high accuracy. These also demonstrate the efficiency and robustness of our SQH-QPAT methodology. We consider a widely varying set of phantoms for D, σ. In Test Case 1, we consider a disk phantom with different intensities for D, σ and investigate reconstruction with the different regularization terms considered in our cost functional J. Next, we discuss two experiments with the heart lung phantom: one in which the relation (9) is satisfied between D and σ, and the other in which (9) is not satisfied, making it a very generic set of phantoms for D, σ. We demonstrate that in both cases, by incorporating the aprior assumption (9) in the functional J, we can obtain high quality reconstructions. We conclude our set of experiments with the

more challenging set of two Shepp-Logan phantoms: the standard one, and another augmented with tumor structures. In the test cases with the heart and lung phantom and the Shepp-Logan phantom, we also implement our method on data containing additive Gaussian noise in order to demonstrate the robustness of our framework.

For the experiments below, we first remark that the units of the spatial variable x is cm and of the absorption coefficient is cm^{-1}. Starting with an experimental square domain of side length 5 cm, we first scale and translate the diffusion equation (6), such that the domain $\Omega = (-1,1) \times (-1,1)$, is discretized into 100 equally spaced points in both the coordinate directions. The corresponding scaling is 1 experimental unit corresponds to 2.5 cm. Thus, based on Table 1, an experimental range of 0-1 for σ_a corresponds to 0-0.4 cm^{-1}. The two boundary radiation functions are $g_1(x,y) = e^x,\ g_2(x,y) = e^y$. The weights of the functional J given in (8) are chosen as $\alpha = 1, \xi_1 = 0.01, \xi_2 = 20, \gamma = 0.01$ and $\Gamma = 1.0$. The large value of ξ_2 is chosen to emphasize the need to satisfy the relation between the diffusion and the absorption coefficient, given by (9), in the numerical experiments. The value of c in the Kubelka-Munk relation (9) is chosen to be $100/3$, though as we have mentioned earlier, this choice is not essential. The initial value of $\epsilon = 10$ and the value of the stopping criteria for convergence is chosen as $\kappa = 10^{-6}$. To generate the data $G_i^\delta,\ i = 1,2$, we first solve for u_i in (6) with given test values of D, σ and boundary illumination data g_i on a finer mesh with $N = 400$ using the cell-nodal finite difference model described in Section 4. We next compute G_i^δ on the finer mesh using the values of σ, σ_b, u_i from (7). We finally restrict the resulting G_i^δ onto the coarser mesh with $N = 100$ and take this as our given data.

To quantify the comparisons of the reconstructions obtained in terms of their contrast (function values) and resolution (discontinuities or edges), with and without noise in the data, we use the following quantitative figures of merit [39]

$$\begin{aligned} &\text{Relative mean square error (RMSE) percentage} = \frac{\|f_{\text{rec}} - f_{\text{ex}}\|_2}{\|f_{\text{ex}}\|_2} * 100\%, \\ &\text{Peak signal-to-noise ratio (PSNR)} = 10 \log_{10} \left(\frac{\max f_{\text{ex}}}{\|f_{\text{rec}} - f_{\text{ex}}\|_2^2} \right), \end{aligned} \tag{22}$$

where f_{ex} is the exact phantom and f_{rec} is the reconstructed phantom.

Test Case 1: we consider a phantom represented by a disk centered at $(0.25, 0.25)$ and having radius 0.25. The value of σ inside the disk is 1 and outside is 0. The background value σ_b is chosen to be 0.16. The corresponding value of D is chosen as 0.003 inside the disk and 0.02 outside. The plots of the actual phantoms for D and the total absorption coefficient σ_a are shown in Figure 1.

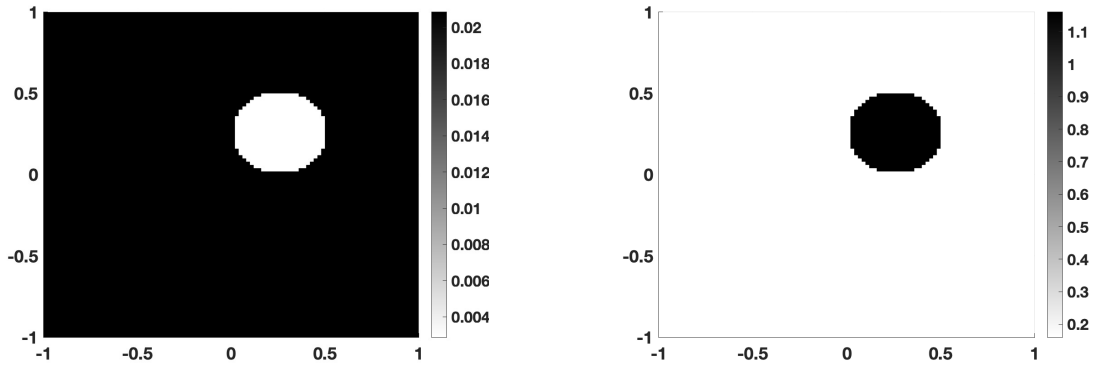

(a) Exact D (b) Exact σ_a

Figure 1: Test Case 1: Exact D and σ represented by disk phantoms.

In Figure 2, we present the reconstruction of D and σ_a using various choices of the regularization terms in J. The first column of images depicts reconstructions of D and σ_a by setting the weight $\xi_2 = 0$ of the regularization term $\left\|D - \bar{D}\right\|_2^2$, which is the term that measures the deviation of D from the Kubelka-Munk approximation $\bar{D}$, given in (9). We see that the reconstruction of D has a very poor resolution and contrast and in turn, this causes loss of contrast in the reconstruction of σ_a. In the second column, we use our regularization term $\left\|D - \bar{D}\right\|_2^2$ but setting the weight $\gamma = 0$ of the sparsity that promotes the L^1 regularization of σ. We now see a reconstructed σ_a with a poor contrast with respect to the background σ_b. The reconstructed D is now far more superior than in the previous cases, but there is still a significant loss of contrast.

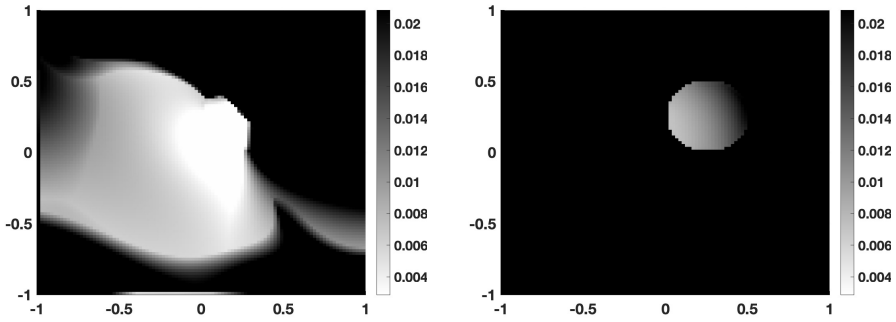

(a) Reconstruction of D with $\alpha = 1, \xi_1 = 0.01, \xi_2 = 0, \gamma = 0.01$

(b) Reconstruction of D with $\alpha = 1, \xi_1 = 0.01, \xi_2 = 20, \gamma = 0$

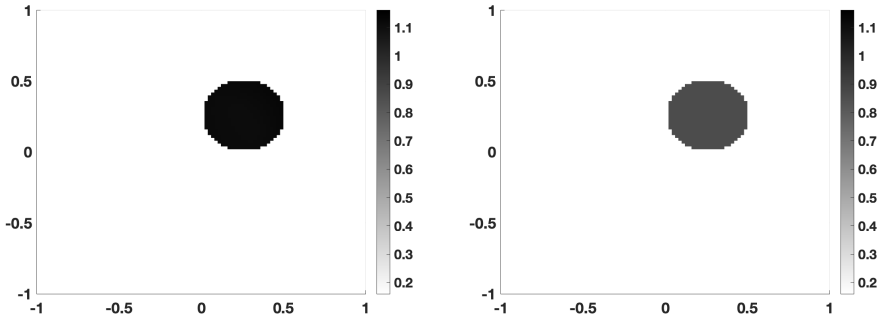

(c) Reconstruction of σ_a with $\alpha = 1, \xi_1 = 0.01, \xi_2 = 0, \gamma = 0.01$

(d) Reconstruction of σ_a with $\alpha = 1, \xi_1 = 0.01, \xi_2 = 20, \gamma = 0$

Figure 2: Test Case 1: The reconstructed disk phantoms with different choices of the values of the regularization weights.

Next, we show that in order to enhance contrast and resolution in the reconstruction, we need to have the L^2 regularization term $\left\|D - \bar{D}\right\|_2^2$ for D and the sparsity promoting L^1 regularization term for σ. In this setting, Figure 3 shows the reconstructions of D and σ_a with our framework using the SQH algorithm. We see that the reconstructed functions are of high resolution and high contrast when compared to the actual phantoms in Figure 1. We also compute the RMSE percentages and PSNR values for the reconstructions in Table 2. We observe that without the Kubelka-Munk regularization term for D and without the L^1 regularization term for σ, we have very high values of RMSE % and low values of PSNR values. With those regularization terms, using the SQH algorithm, we obtain RMSE % of around 1 and high PSNR values, reaffirming the superiority of the reconstructions.

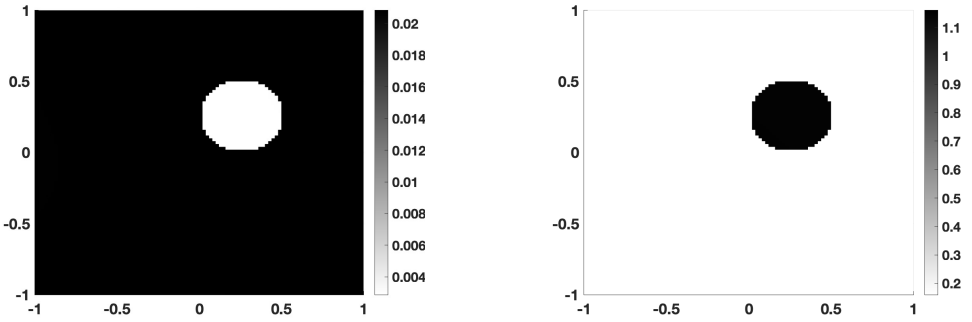

(a) Reconstruction of D with $\alpha = 1, \xi_1 = 0.01, \xi_2 = 20, \gamma = 0.01$

(b) Reconstruction of σ_a with $\alpha = 1, \xi_1 = 0.01, \xi_2 = 20, \gamma = 0.01$

Figure 3: Test Case 1: The reconstructed disk phantoms using the weights $\alpha = 1, \xi_1 = 0.01, \xi_2 = 20, \gamma = 0.01$.

Method	RMSE % (D)	RMSE % (σ_a)	PSNR (D)	PSNR (σ_a)
Without Kubelka-Munk ($\xi_2 = 0$)	225.7	9.24	25.09	32.37
Without L^1 ($\gamma = 0$)	218	30.47	27.06	23.51
With Kubelka-Munk ($\xi_2 = 20$) and L^1 ($\gamma = 0.01$)	0.08	1.41	94.33	50.29

Table 2: Test Case 1: RMSE % and PSNR values for reconstructions of the disk phantom with different regularization weights

Test Case 2: we demonstrate the robustness of our framework for reconstructing multiple objects. In this test case, we consider a heart lung phantom for σ. The underlying value of the phantom is 0 that is perturbed into two ellipses that represent the lungs with value 1, and a disk representing the heart with value 0.5. The value of σ_b is chosen to be 0.03. The value of D is chosen as 0.003 inside the ellipses, 0.006 inside the disk and 0.1 elsewhere. The plots of the exact and the reconstructed phantoms are shown in Figure 4.

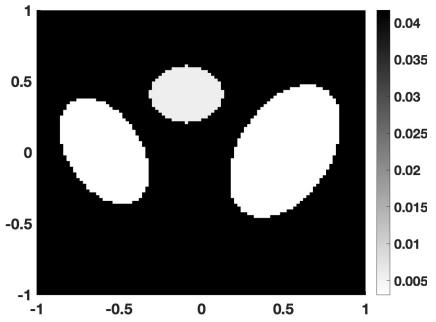

(a) Exact D

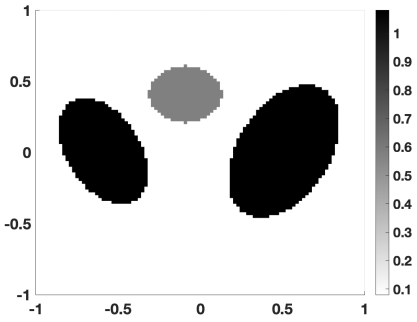

(b) Exact σ_a

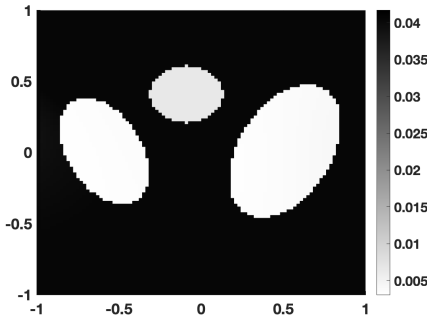

(c) Reconstructed D

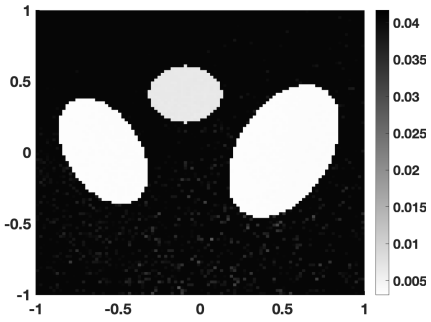

(d) Reconstructed D with 5% noise

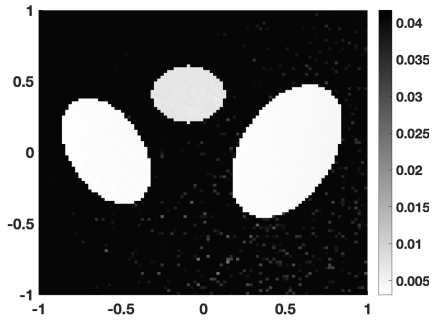

(e) Reconstructed D with 10% noise

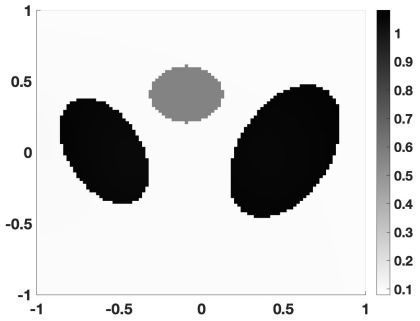

(f) Reconstructed σ_a

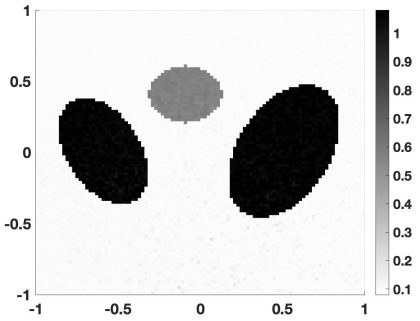

(g) Reconstructed σ_a with 5% noise

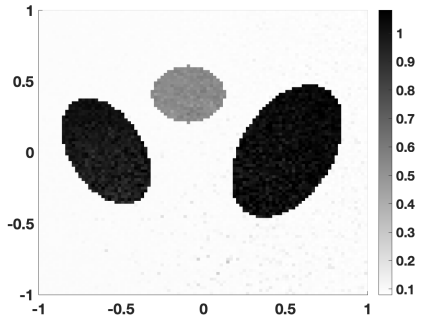

(h) Reconstructed σ_a with 10% noise

Figure 4: Test Case 2: The actual and the reconstructed phantoms

We see from the reconstructed images of D and σ_a in Figures 4c and 4f that they are of high contrast and resolution. Now, in order to test the robustness of our method with noisy data, we introduce 5% and 10% multiplicative Gaussian noise to the interior data $\mathcal{H}$. We also modify the L^2 and L^1 regularization weights for σ, $\xi_1 = 0.1$ and $\gamma = 0.1$. This ensures removal of artifacts from the reconstruction of σ due to the noisy data, which in turn helps to remove some artifacts in the reconstruction of D. Figures 4d, 4e, 4g and 4h show the corresponding reconstructions. We see that the reconstructions of D and σ_a involve a few artifacts near the bottom, more pronounced in the case of 10% noise. But overall, both reconstructions still preserve obtain high contrast and resolution near and at the regions of the heart and lungs. This is also validated analytically from the low RMSE % and high PSNR values of the reconstructions presented in Table 3.

Noise %	RMSE % (D)	RMSE % (σ_a)	PSNR (D)	PSNR (σ_a)
0	2.32	3.42	59.96	34.55
5	2.94	3.46	57.08	33.89
10	2.86	7.56	56.24	28.05

Table 3: Test Case 2: RMSE % and PSNR values for reconstructions of the heart and lung phantom with different noise levels in the data

Test Case 3: we investigate the robustness of our SQH-QPAT algorithm in reconstructing D in the case where the Kubelka-Munk relation (9) is by far not satisfied; i.e. we have factors different from 100. For this test case, in regard to σ, we again consider the setting for heart and lung phantom as described in test Case 2. However, for the value of D, we choose $D = 0.0006$ inside the right ellipse, $D = 0.003$ inside the left ellipse, $D = 0.009$ inside the disk and $D = 0.1$ for the background. The value of σ_b is again chosen to be 0.03.

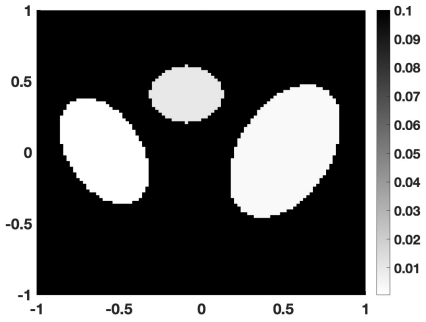

(a) Exact D

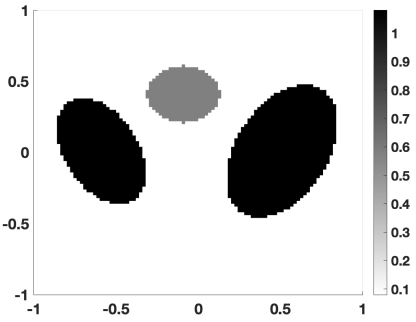

(b) Exact σ_a

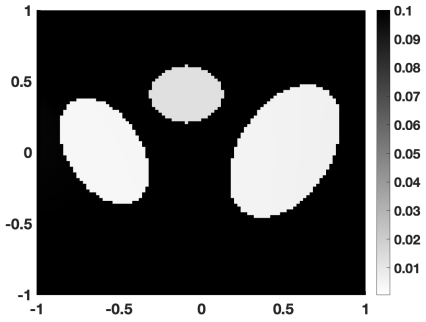

(c) Reconstructed D

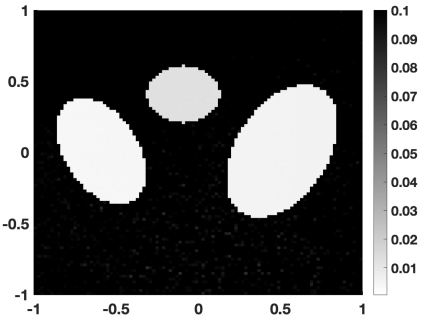

(d) Reconstructed D with 5% noise

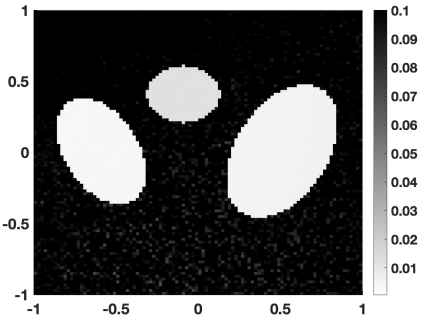

(e) Reconstructed D with 10% noise

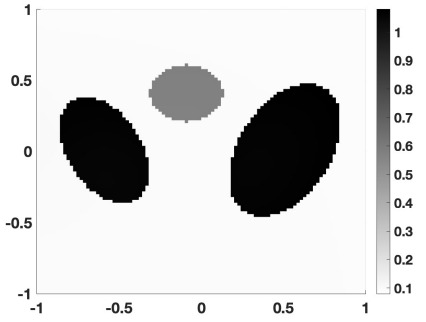

(f) Reconstructed σ_a

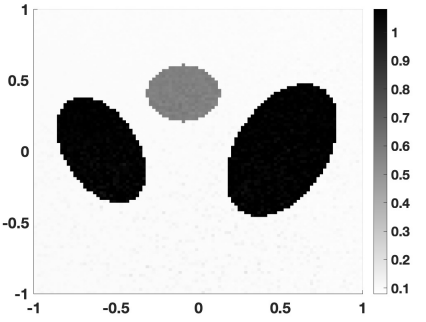

(g) Reconstructed σ_a with 5% noise

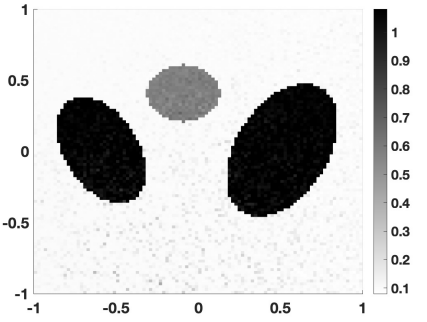

(h) Reconstructed σ_a with 10% noise

Figure 5: Test Case 3: The actual and the reconstructed phantoms

With this challenging setting, we perform our reconstructions of D and σ_a and depict the results in Figure 5 with and without noise in the data. We again observe high contrast and resolution reconstructions of D and σ_a, even in the presence of 5% and 10% noise in the data. The corresponding RMSE % and PSNR values are presented in Table 4, which are similar to the previous test case.

Noise %	RMSE % (D)	RMSE % (σ_a)	PSNR (D)	PSNR (σ_a)
0	1.47	3.25	56.69	35.88
5	1.43	3.57	54.18	34.57
10	2.13	4.61	47.70	30.05

Table 4: Test Case 3: RMSE % and PSNR values for reconstructions of the second heart and lung phantom with different noise levels in the data

Test Case 4: we perform another challenging test using the Shepp-Logan phantom that represents the structure of a human head, which comprises ellipses, disks of varying radii, and an elliptical annulus. In this case, σ has the structure of Shepp-Logan phantom as given in [55]. The phantom is described as follows: The values of σ and D, respectively, inside two big ellipses centered at (0.22,0) and (-0.22,0) are -0.3 and 0.02, inside the big disk centered at (0,0.35) are 0.5 and 0.003, inside the 2 small disks centered at (0,0.1) and (0,-0.1) are 0.5 and 0.003, inside the small ellipses centered at (-0.08,-0.605), (0,-0.606) and (0.06, -0.605) are 0.5 and 0.003, inside the elliptical annulus are 1 and 0.002, and elsewhere 0 and 0.006. The background σ_b is chosen to be 0.5 in this case.

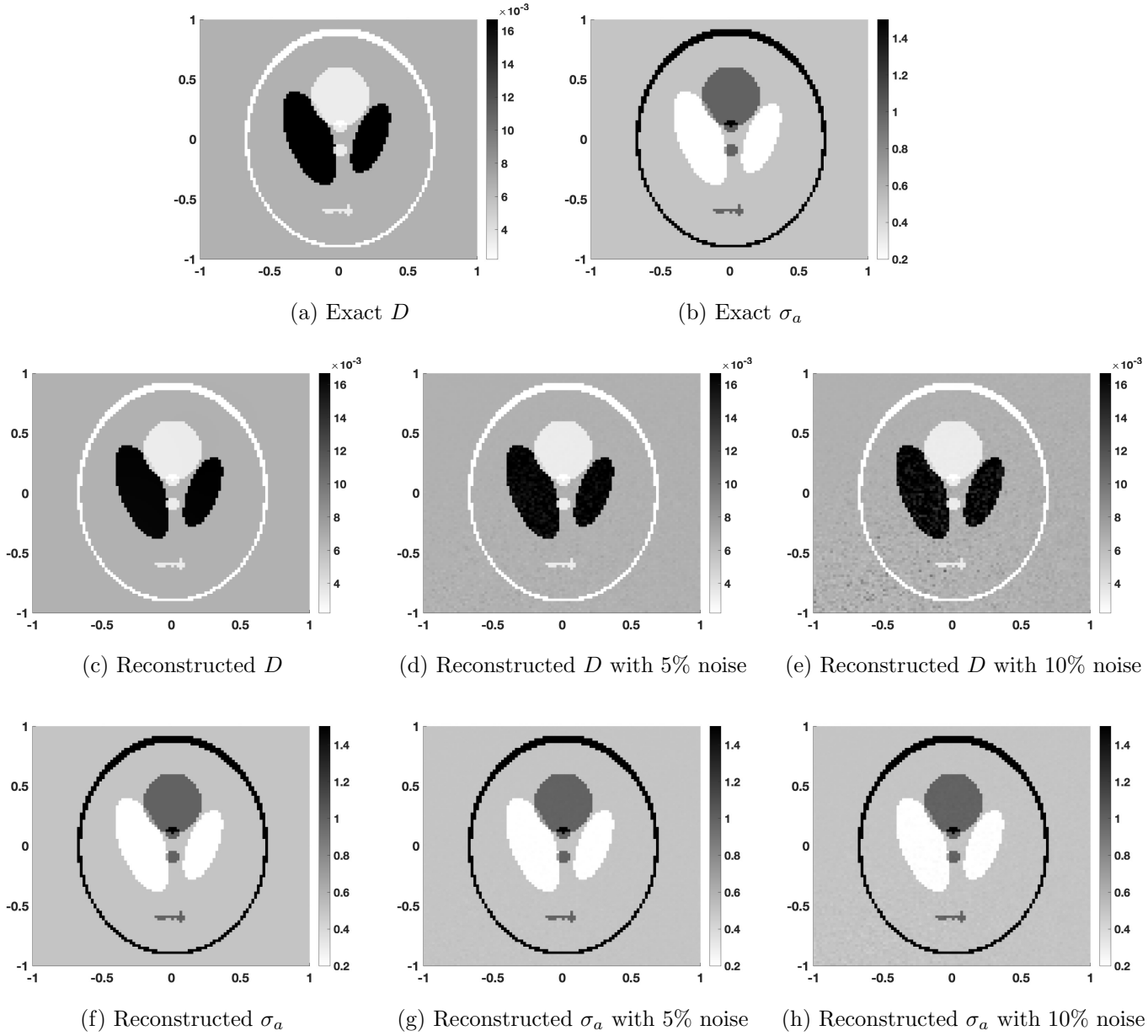

(a) Exact D (b) Exact σ_a

(c) Reconstructed D (d) Reconstructed D with 5% noise (e) Reconstructed D with 10% noise

(f) Reconstructed σ_a (g) Reconstructed σ_a with 5% noise (h) Reconstructed σ_a with 10% noise

Figure 6: Test Case 4: The actual and the reconstructed phantoms

For test Case 4, Figure 6 shows the exact and the reconstructed values of D and σ_a with high resolution and contrast. Figures 6d, 6e and 6g, 6h depict the reconstruction with 5% and 10% multiplicative Gaussian noise in the interior data, respectively. We obtain high quality reconstruction with our SQH-QPAT framework also in the case of objects with holes and inclusions. The corresponding RMSE % and PSNR values are presented in Table 5. We do observe that the RMSE % is higher than in the case of the heart and lung phantom, which is expected since there are far more finer features in the Shepp-Logan phantom. However, the PSNR values are still at a comparable level to the previous test cases that indicate that the reconstructions have high quality.

Noise %	RMSE % (D)	RMSE % (σ_a)	PSNR (D)	PSNR (σ_a)
0	16.21	6.54	55.89	38.57
5	16.36	6.68	55.80	38.02
10	16.58	6.71	55.47	36.31

Table 5: Test Case 4: RMSE % and PSNR values for reconstructions of the Shepp-Logan phantom with different noise levels in the data

Test Case 5: while in the previous test cases the phantoms to be reconstructed represented organs in a human being, in this test case, we present results of detecting a tumor along with organs using our SQH-QPAT framework. We consider σ that represents the organs as the same Shepp-Logan phantom of test Case 4. The σ for the tumors are represented by two disks: one of them having a large contrast with value 1.5 and the other having a contrast similar to the some of the organs with value 0.2. The corresponding value of D is 0.001 and 0.004, respectively. The background value $\sigma_b = 0.5$.

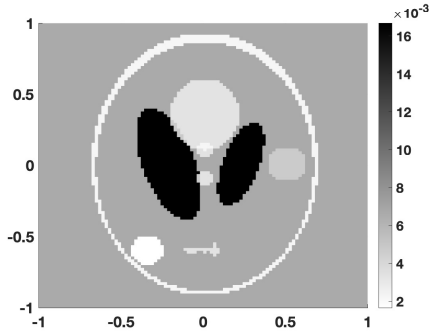

(a) Exact D

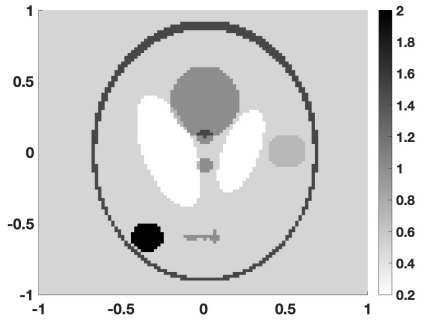

(b) Exact σ_a

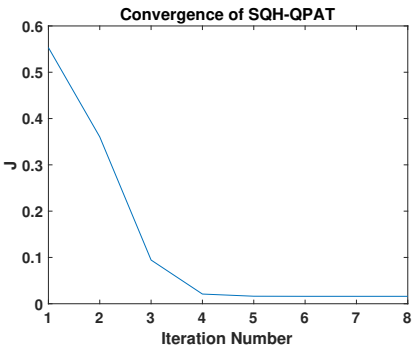

(c) Convergence history of SQH-QPAT iteration

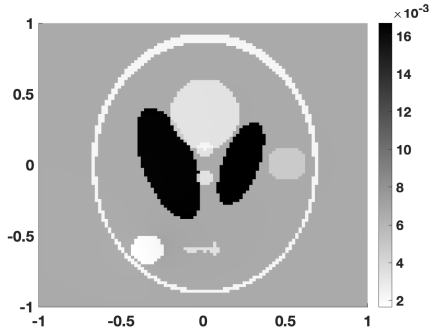

(d) Reconstructed D

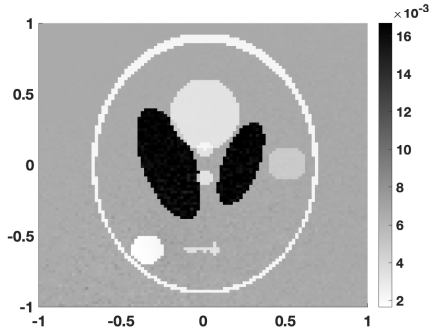

(e) Reconstructed D with 5% noise

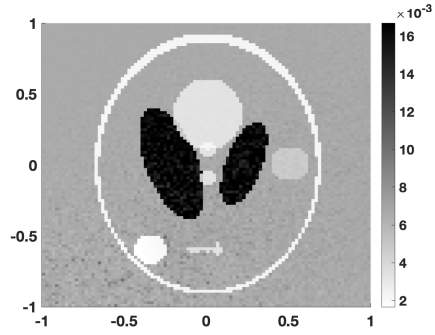

(f) Reconstructed D with 10% noise

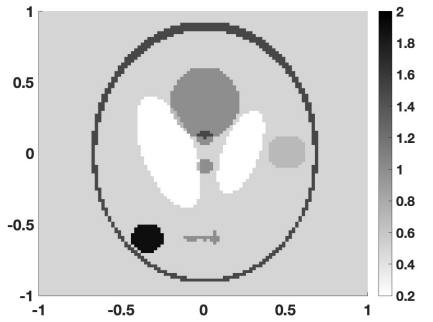

(g) Reconstructed σ_a

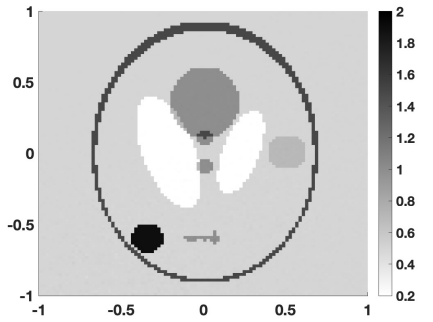

(h) Reconstructed σ_a with 5% noise

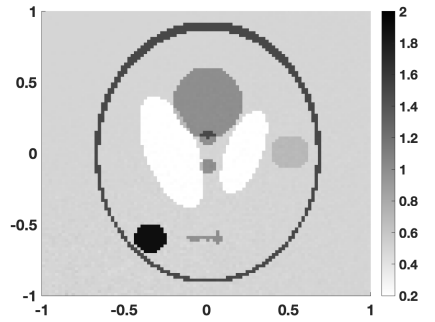

(i) Reconstructed σ_a with 10% noise

Figure 7: Test Case 5: The actual and the reconstructed phantoms

For test Case 5, Figure 7 shows the exact and the reconstructed values of D and σ_a with and without noise in the interior data. We see that our SQH-QPAT framework is able to reconstruct very well the tumors alongside the organs, which further demonstrates the wide applicability of our reconstruction framework. Figure 7c shows the convergence history of the SQH-QPAT scheme. Notice the strict monotonic decrease in the functional values, with stopping criteria fulfilled in 8 iterations. From Table 6, we also observe similar RMSE % and PSNR values, as in the previous test case, demonstrating high quality reconstructions.

Noise %	RMSE % (D)	RMSE % (σ_a)	PSNR (D)	PSNR (σ_a)
0	16.50	7.19	55.89	36.62
5	16.69	7.40	55.79	36.25
10	16.90	7.40	55.45	35.12

Table 6: Test Case 5: RMSE % and PSNR values for reconstructions of the Shepp-Logan phantom with different noise levels in the data

6 Conclusion

A new optimization framework for reconstruction with high contrast and resolution of optical diffusion and absorption coefficients in quantitative photoacoustic tomography (QPAT) was presented. The resulting QPAT inverse problem was formulated as the minimization of a best-fit functional with a tentative prior relating the diffusion and absorption coefficients and L^2 and L^1 regularization terms, and subject to the constraint of the steady photon-propagation equation.

For the solution of this problem, a robust and fast sequential quadratic hamiltonian algorithm based on the Pontryagin maximum principle was developed and analysed. Results of numerical experiments were presented that demonstrate the ability of the proposed framework to efficiently compute reconstructions of the optical coefficients with high contrast and resolution.

Acknowledgments

This work was partially supported by the German BMBF-Project iDeLIVER : Intelligent MR Diagnosis of the Liver by Linking Model and Data-Driven Processes, and by the US National Science Foundation Grant No: 2309491, and the University of Texas at Arlington, Research Enhancement Program Grant No: 2022-605.

A Proof of Theorem 4.1

We have

$$H_\epsilon(x,y,D,\sigma,D^k,\sigma^k,u_1^k,u_2^k,q_1^k,q_2^k) \le H_\epsilon(x,y,w,z,D^k,\sigma^k,u_1^k,u_2^k,q_1^k,q_2^k)$$

for all $w \in [D_l, D_r],\ z \in [\sigma_l, \sigma_r]$. Hence, it follows that

$$\begin{aligned} H_\epsilon(x,y,D,\sigma,D^k,\sigma^k,u_1^k,u_2^k,q_1^k,q_2^k) \le & H_\epsilon(x,y,D^k,\sigma^k,D^k,\sigma^k,u_1^k,u_2^k,q_1^k,q_2^k) \\ = & H(x,y,D^k,\sigma^k,u_1^k,u_2^k,q_1^k,q_2^k) \end{aligned} \tag{23}$$

for all $(x,y) \in \Omega$. Let

$$\begin{aligned} L(x,y,D,\sigma,u_1,u_2) = & \frac{\alpha}{2}\sum_{i=1}^{2}(\mathcal{H}(x,y,\sigma,u_i) - G_i^\delta(x,y))^2 + \frac{\xi_1}{2}\sigma^2(x,y) \\ & + \frac{\xi_2}{2}\left(D(x,y) - \frac{1}{100\ (\sigma(x,y)+\sigma_b)}\right)^2 + \gamma|\sigma(x,y)|. \end{aligned}$$

Then, we have

$$J(D,\sigma,u_1,u_2) - J(D^k,\sigma^k,u_1^k,u_2^k) = \int_\Omega L(x,y,D,\sigma,u_1,u_2) - L(x,y,D^k,\sigma^k,u_1^k,u_2^k)\ dxdy. \quad (24)$$

Adding and subtracting $D^k\ \nabla q_i^k \cdot \nabla u_i + (\sigma^k + \sigma_b)\ q_i^k u_i$ and $D^k\ \nabla q_i^k \cdot \nabla u_i^k + (\sigma^k + \sigma_b)\ q_i^k u_i^k$ to the right-hand side of (24), we obtain

$$\begin{aligned}
&J(D,\sigma,u_1,u_2) - J(D^k,\sigma^k,u_1^k,u_2^k)\\
&= \int_\Omega L(x,y,D,\sigma,u_1,u_2)\ dxdy + \int_\Omega \sum_{i=1}^{2} \left(D^k\ \nabla q_i^k \cdot \nabla u_i + (\sigma^k + \sigma_b)\ q_i^k u_i\right)\ dxdy\\
&\quad - \int_\Omega \sum_{i=1}^{2} \left(D^k\ \nabla q_i^k \cdot \nabla u_i + (\sigma^k + \sigma_b)\ q_i^k u_i\right)\ dxdy\\
&\int_\Omega - L(x,y,D^k,\sigma^k,u_1^k,u_2^k)\ dxdy - \int_\Omega \sum_{i=1}^{2} \left(D^k\ \nabla q_i^k \cdot \nabla u_i^k + (\sigma^k + \sigma_b)\ q_i^k u_i^k\right)\ dxdy\\
&\quad + \int_\Omega \sum_{i=1}^{2} \left(D^k\ \nabla q_i^k \cdot \nabla u_i^k + (\sigma^k + \sigma_b)\ q_i^k u_i^k\right)\ dxdy.
\end{aligned}$$

This gives us

$$\begin{aligned}
&J(D,\sigma,u_1,u_2) - J(D^k,\sigma^k,u_1^k,u_2^k)\\
&= \int_\Omega H(x,y,D,\sigma,u_1,u_2,q_1^k,q_2^k) - H(x,y,D^k,\sigma^k,u_1^k,u_2^k,q_1^k,q_2^k) - \sum_{i=1}^{2} \left(D^k\ \nabla q_i^k \cdot \nabla u_i + (\sigma^k + \sigma_b)\ q_i^k u_i\right)\\
&\quad + \sum_{i=1}^{2} \left(D^k\ \nabla q_i^k \cdot \nabla u_i^k + (\sigma^k + \sigma_b)\ q_i^k u_i^k\right)\ dxdy.\\
&= \int_\Omega H(x,y,D,\sigma,u_1^k + \delta u_1, u_2^k + \delta u_2, q_1^k, q_2^k) - H(x,y,D^k,\sigma^k,u_1^k,u_2^k,q_1^k,q_2^k)\\
&\quad - \sum_{i=1}^{2} \left(D^k\ \nabla q_i^k \cdot \nabla u_i + (\sigma^k + \sigma_b)\ q_i^k u_i\right) + \sum_{i=1}^{2} \left(D^k\ \nabla q_i^k \cdot \nabla u_i^k + (\sigma^k + \sigma_b)\ q_i^k u_i^k\right)\ dxdy.\\
&= \int_\Omega H(x,y,D,\sigma,u_1^k,u_2^k,q_1^k,q_2^k) + \Gamma\alpha \sum_{i=1}^{2} \left[-(\sigma^k + \sigma_b)[\mathcal{H}(x,y,\sigma^k,u_i^k) - G_i^\delta]\delta u_i + \frac{1}{2}(\sigma^k + \sigma_b)(\delta u_i)^2\right]\\
&\quad - H(x,y,D^k,\sigma^k,u_1^k,u_2^k,q_1^k,q_2^k) - \sum_{i=1}^{2} \left(D^k\ \nabla q_i^k \cdot \nabla u_i + (\sigma^k + \sigma_b)\ q_i^k u_i\right)\\
&\quad + \sum_{i=1}^{2} \left(D^k\ \nabla q_i^k \cdot \nabla u_i^k + (\sigma^k + \sigma_b)\ q_i^k u_i^k\right)\ dxdy
\end{aligned}$$

$$
\begin{aligned}
&= \int_\Omega H(x,y,D,\sigma,u_1^k,u_2^k,q_1^k,q_2^k) + \epsilon[(\delta D)^2+(\delta\sigma)^2] - H(x,y,D^k,\sigma^k,u_1^k,u_2^k,q_1^k,q_2^k)\; dxdy \\
&\quad + \int_\Omega \sum_{i=1}^{2} \left\{ \Gamma\alpha(\sigma^k+\sigma_b)[\mathcal{H}(x,y,\sigma^k,u_i^k) - G_i^\delta]u_i + \left(D^k\ \nabla q_i^k \cdot \nabla u_i + (\sigma^k+\sigma_b)\ q_i^k u_i\right) \right\} dxdy \\
&\quad - \int_\Omega \sum_{i=1}^{2} \left\{ \Gamma\alpha(\sigma^k+\sigma_b)[\mathcal{H}(x,y,\sigma^k,u_i^k) - G_i^\delta]u_i^k + \left(D^k\ \nabla q_i^k \cdot \nabla u_i^k + (\sigma^k+\sigma_b)\ q_i^k u_i^k\right) \right\} dxdy \\
&\quad + \sum_{i=1}^{2} \int_\Omega \frac{1}{2}(\sigma^k+\sigma_b)(\delta u_i)^2 - \epsilon\left[(\delta D)^2+(\delta\sigma)^2\right] dxdy \\
&= \int_\Omega H_\epsilon(x,y,D,\sigma,D^k,\sigma^k,u_1^k,u_2^k,q_1^k,q_2^k) - H(x,y,D^k,\sigma^k,u_1^k,u_2^k,q_1^k,q_2^k)\; dxdy \\
&\quad + \sum_{i=1}^{2} \int_\Omega \frac{1}{2}(\sigma^k+\sigma_b)(\delta u_i)^2\; dxdy - \int_\Omega \epsilon\left[(\delta D)^2+(\delta\sigma)^2\right] dxdy, \qquad \text{(using (15))} \\
&\leq \sum_{i=1}^{2} \int_\Omega \frac{1}{2}(\sigma^k+\sigma_b)(\delta u_i)^2\; dxdy - \int_\Omega \epsilon\left[(\delta D)^2+(\delta\sigma)^2\right] dxdy, \qquad \text{(using (23))}
\end{aligned}
$$

Now, we recall the result of Lemma 3.1 that gives the following

$$\|\delta u_i\|^2_{L^2(\Omega)} \leq \bar{C}_1 \left(\|\delta D\|^2_{L^2(\Omega)} + \|\delta\sigma\|^2_{L^2(\Omega)}\right),$$

where $\bar{C}_1 = 2\,c_3^2/c_1^2$. Hence, we proceed as follows

$$
\begin{aligned}
J(D,\sigma,u_1,u_2) - J(D^k,\sigma^k,u_1^k,u_2^k) &\leq \int_\Omega -\epsilon\left[(\delta D)^2+(\delta\sigma)^2\right]\; dxdy + \sum_{i=1}^{2}\int_\Omega \frac{1}{2}(\sigma^k+\sigma_b)(\delta u_i)^2\, dx \\
&\leq -\epsilon\left[\|\delta D\|^2_{L^2(\Omega)} + \|\delta\sigma\|^2_{L^2(\Omega)}\right] + \sum_{i=1}^{2}\frac{\bar{\sigma}}{2}\|\delta u_i\|^2_{L^2(\Omega)} \\
&\leq -\epsilon\left[\|\delta D\|^2_{L^2(\Omega)} + \|\delta\sigma\|^2_{L^2(\Omega)}\right] + \bar{C}_1\,\bar{\sigma}\ \left[\|\delta D\|^2_{L^2(\Omega)} + \|\delta\sigma\|^2_{L^2(\Omega)}\right] \\
&= -\left(\epsilon - \bar{C}_1\,\bar{\sigma}\right)\ \left[\|\delta D\|^2_{L^2(\Omega)} + \|\delta\sigma\|^2_{L^2(\Omega)}\right],
\end{aligned}
$$

where $\bar{\sigma} = \sigma_r + \sigma_b$. Thus, the theorem is proved with $\theta = \bar{C}_1\,\bar{\sigma}$.

References

[1] G. S. Abdoulaev, K. Ren and A. H. Hielscher. Optical tomography as a PDE-constrained optimization problem, *Inverse Problems*, 21:1507-1530, 2005.

[2] B. Adesokan, K. Knudsen, V. P. Krishnan and S. Roy. A fully non-linear optimization approach to acousto-electric tomography. *Inverse Problems*, 34:104004, 2018.

[3] G. S. Alberti and Y. Capdeboscq. Lectures on Elliptic Methods for Hybrid Inverse Problems, Société Mathématique de France, Paris, 2018.

[4] A. Borzì and V. Schulz. Computational optimization of systems governed by partial differential equations, *SIAM Computational Science and Engineering*, 2012.

[5] H. W. Alt. Linear Functional Analysis. An Application-Oriented Introduction, Springer, 2016.

[6] R. Aronson and N. Corngold. Photon diffusion coefficient in an absorbing medium, *Journal of Optical Society of America*, 16(5):1066-1071, 1999.

[7] U. M. Ascher and E. Haber, A multigrid method for distributed parameter estimation problems, *ETNA*, 18 (2003), 1-18.

[8] H. Ammari, E. Bossy, V. Jugnon and H. Kang. Reconstruction of the optical absorption coefficient of a small absorber from the absorbed energy density, *SIAM Journal of Applied Mathematics*, 71:676-693, 2011.

[9] S. R. Arridge. Optical tomography in medical imaging, *Inverse Problems*, R41-R93, 1999.

[10] G. Bal, A. Jollivet and V. Jugnon. Inverse transport theory of photoacoustics, *Inverse Problems*, 26(2):025011, 2010.

[11] G. Bal and K. Ren. Multi-source quantitative photoacoustic tomography in a diffusive regime, *Inverse Problems*, 27:075003, 2011.

[12] G. Bal and K. Ren. On multi-spectral quantitative photoacoustic tomography in diffusive regime, *Inverse Problems*, 28:025010, 2012.

[13] G. Bal and G. Uhlmann. Inverse diffusion theory of photoacoustics, *Inverse Problems*, 26:085010, 2010.

[14] G. Bal and G. Uhlmann. Reconstruction of coefficients in scalar second-order elliptic equations from knowledge of their solutions, *Communications in Pure and Applied Mathematics*, 66:1692-1752, 2013.

[15] B. Banerjee, S. Bagchi, R. M. Vasu and D. Roy. Quantitative photoacoustic tomography from boundary pressure measurements: noniterative recovery of optical absorption coefficient from the reconstructed absorbed energy map, *Journal of Optical Society of America A*, 25(9):2347-2356, 2008.

[16] H.T. Banks and K. Kunisch. Estimation Techniques for Distributed Parameter Systems, Birkhäuser, Basel, 1989.

[17] N. Bosschaart, G. J. Edelman, M. C. G. Aalders, T. G. van Leeuwen and D. J. Faber. *A literature review and novel theoretical approach on the optical properties of whole blood, Lasers in Medical Science*, 29:453–479, 2014.

[18] T. Breitenbach and A. Borzì. A sequential quadratic Hamiltonian method for solving parabolic optimal control problems with discontinuous cost functionals, *Journal of Dynamical and Control Systems*, 25(3):1-33, 2018.

[19] T. Breitenbach and A. Borzì. On the SQH Scheme to solve nonsmooth PDE optimal control problems, *Numerical Functional Analysis and Optimization*, 40(13): 1489-1531, 2019.

[20] T. Breitenbach and A. Borzì. A sequential quadratic Hamiltonian scheme for solving nonsmooth quantum control problems with sparsity, *Journal of Computational and Applied Mathematics*, 369:112583, 2019.

[21] F. L. Chernous'ko, A. A. Lyubushin. Method of successive approximations for solution of optimal control problems, *Optimal Control Applications and Methods*, 3(2):101 - 114, 2007.

[22] A. Cianchi and V. Maz'ya. Global gradient estimates in elliptic problems under minimal data and domain regularity. *Communications on Pure & Applied Analysis*, 14:285, 2015.

[23] F. H. Clarke. Optimization and Nonsmooth Analysis. *John Wiley & Sons, New York*, 1983.

[24] B. T. Cox, S. R. Arrdige, P. Köstli and P. C. Beard. Two-dimensional quantitative photoacoustic image reconstruction of absorption distributions in scattering media by use of a simple iterative method, *Applied Optics*, 45:1866-1875, 2006.

[25] B. T. Cox, S. R. Arrdige and P. C. Beard. Estimating chromophore distributions from multiwavelength phtoacoustic images, *Journal of Optical Society of America*, 26:443-455, 2009.

[26] A. Dimofte, J. Finlay and T. Zhu. A method for determination of the absorption and scattering properties interstitially in turbid media, *Physics in Medicine and Biology*, 50(10): 2291–2311, 2005.

[27] D. J. Durian. The diffusion coefficient depends on absorption, *Optics Letters*, 23(19):1502-1504, 1998.

[28] V. Dzimbeg-Malcic, Zeljka Barbaric-Mikocevic and Katarina Itric. Kubelka-Munk theory in describing optical properties of paper (I), *Tehnicki Vjesnik*, 19(1):191-196, 2012.

[29] F. Fanjul-Vélez, S. Pampín-Suárez and J. L. Arce-Diego. Application of classification algorithms to diffuse reflectance spectroscopy measurements for ex vivo characterization of biological tissues, *Entropy*, 22:736, 2020.

[30] A diffusion theory model of spatially resolved, steady-state diffuse reflectance for the noninvasive determination of tissue optical properties in vivo, *Medical Physics*, 19(4):879-888, 1992.

[31] D. Finch and Rakesh. Recovering a function from its spherical mean values in two and three dimensions, *Photoacoustic Imaging and Spectroscopy, ed. L. H. Wang*, CRC Press, 2009.

[32] D. Gao, Y. Liu, Y. Wang and Z. Yuan. Protein-modified ultra-small gold clusters for dual-modal in vivo fluorescence/photoacoustic imaging, *Quantitative Imaging in Medicine and Surgery*, 8(3):326-332, 2018.

[33] H. Gao, J. Feng and L. Song. Limited-view multi-source quantitative photoacoustic tomography, *Inverse Problems*, 31:065004, 2015.

[34] H. Gao, S. Osher and H. Zhao. Quantitative photoacoustic tomography, *Mathematical Modeling in Biomedical Imaging II, Lecture Notes in Mathematics 2035, Springer, Heidelberg*, 131-158, 2012.

[35] D. Gilbarg and N. Trudinger. Elliptic Partial Differential Equations of Second Order. Springer-Verlag Berlin Heidelberg New York, 1998.

[36] M. Haltmeier, L. Neumann, L. Nguyen and S. Rabanser. Analysis of the linearized problem of quantitative photoacoustic tomography, *SIAM Journal of Applied Mathematics*, 78(1):457-478, 2018.

[37] H. G. Hecht. The interpretation of diffuse reflectance spectra, *Journal of Research of the National Bureau of Standards-A. Physics and Chemistry*, 80A(4):567-583, 1976.

[38] A. Ishimaru. Wave Propagation and Scattering in Random Media , New York, Academic Press, 1978.

[39] P. E. Kinahan and J. S. Karp. Figures of merit for comparing reconstruction algorithms with a volume-imaging PET scanner, *Physics in Medicine and Biology*, 39(3):631-642, 1994.

[40] P. Kuchment and D. Steinhauer. Stabilizing inverse problems by internal data, *Inverse Problems*, 28(8):084007, 2012.

[41] P. Kubelka and F. Munk. Ein Beitrag zur Optik der Farbanstriche, *Z. Tech. Phys.*, 12:593-601, 1931.

[42] O. A. Ladyzhenskaya and N. N. Ural'tseva. Linear and Quasilinear Elliptic Equations, *Academic Press, New York and London*, 1968.

[43] J. Laufer, B. Cox, E. Zhang and P. Beard. Quantitative determination of chromophore concentrations from 2d photoacoustic images using a nonlinear model-based inversion scheme, *Applied Optics*, 49:1219-1233, 2010.

[44] R. Leitao and E. Teixeira. Regularity and geometric estimates for minima of discontinuous functionals, *Rev. Mat. Iberoam*, 31(1):69-108, 2015.

[45] G. Mingione. Regularity of minima: An invitation to the dark side of the calculus of variations, Applications of Mathematics, 51:355-426, 2006.

[46] V. Ntziachristos, Fluorescence molecular imaging, *Annual Review of Biomedical Engineering*, 8:1-33, 2006.

[47] K. Ren, H. Gao and H. Zhao. A hybrid reconstruction method for quantitative PAT, *SIAM Journal of Imaging Sciences*, 6:32-55, 2013.

[48] A. Roy, R. Ramasubramaniam and H. A. Gaonkarb. Empirical relationship between Kubelka–Munk and radiative transfer coefficients for extracting optical parameters of tissues in diffusive and nondiffusive regimes, *Journal of Biomedical Optics*, 17(11):115006, 2012.

[49] S. Roy and A. Borzì. A new optimisation approach to sparse reconstruction of log-conductivity in acousto-electric tomography, *SIAM Journal on Imaging Sciences*, 11(2):1759–1784, 2018.

[50] Y. Sakawa and Y. Shindo. On global convergence of an algorithm for optimal control. *IEEE Transactions on Automatic Control*, 25(6):1149–1153, 1980.

[51] J. L. Sandell and T. C. Zhu. A review of in-vivo optical properties of human tissues and its impact on PDT, *Journal of Biophotonics*, 4(11-12): 773–787, 2011.

[52] T. Saratoon, T. Tarvainen, B. T. Cox and S. R. Arrdige. A gradient-based method for quantitative photoacoustic tomography using the radiative transfer equation, *Inverse Problems*, 29:075006, 2013.

[53] J. C. Schotland, Direct reconstruction methods in optical tomography, *Lecture Notes in Mathematics, Vol. 2035, Springer-Verlag, Berlin*, 1-29, 2011.

[54] P. Shao, B. Cox and R. J. Zemp. Estimating optical absorption, scattering, and Grueneisen distributions with multiple-illumination photoacoustic tomography, *Applied Optics*, 50:3145-3154, 2011.

[55] L. A. Shepp and B. F. Logan. The Fourier reconstruction of a head section. *IEEE Transactions on Nuclear Science*, 21(3):21–43, 1974.

[56] G. Stadler. Elliptic optimal control problems with L^1-control cost and applications for the placement of control devices, *J Comp Opt and App*, 44:159-181, 2007.

[57] Light scattering methods for tissue diagnosis, *Optica*, 6(4):479-489, 2019.

[58] M.I. Sumin. Optimal control of objects described by quasilinear elliptic equations, *Differ. Equations*, 25: 1004-1012, 1989.

[59] T. Tarvainen, B. T. Cox, J. P. Kaipio and S. R. Arridge. Reconstructing absorption and scattering distributions in quantitative photoacoustic tomography, *Inverse Problems*, 28:084009, 2012.

[60] M. Ulbrich. Semismooth Newton Methods for Variational Inequalities and Constrained Optimization Problems in Function Spaces, SIAM, Philadelphia, 2011.

[61] L. V. Wang. Multiscale photoacoustic microscopy and computed tomography, *Nature Photonics*, 3:503-509, 2009.

[62] H-J. Wei, D. Xing, G-Y. Wu, Y. Jin and H-M. Gu. Optical properties of human normal small intestine tissue determined by Kubelka-Munk method in vitro, *World Journal of Gastroenterology*, 9(9):2068-2072, 2003.

[63] J. Xia, J. Yao, and L. V. Wang. Photoacoustic tomography: principles and advances, *Electromagnetic Waves*, 147:1-22, 2014.

[64] L. Yao, Y. Sun and H. Jiang. Transport-based quantitative photoacoustic tomography: simulations and experiments, *Physics in Medicine and Biology*, 55:1917-1934, 2010.

[65] R. J. Zemp. Quantitative photoacoustic tomography with multiple optical sources, *Applied Optics*, 49:3566-3572, 2010.